Mass-Transfer Effects of Bubble Streams Rising Near Vertical Electrodes

Mass-transfer enhancement by a stream of bubbles rising near a planar, vertical surface is resolved spatially and temporally using a micromosaic electrode. A stream of gas bubbles is generated electrolytically, either at a segment directly below and in the plane of the monitoring electrodes, or at a wire tip that can be positioned inside or outside the mass-transfer boundary layer. The mass-transfer enhancement resulting from bubbles rising within the mass-transfer boundary layer is found to be strong and localized, in agreement with trends predicted by a surface-renewal model. Mass transfer resulting from bubbles rising outside the boundary layer is found to receive a steady, laminar enhancement, correlating well with predictions from an idealization of the bubble stream entraining a cylinder of liquid.

Gina M. Whitney
Charles W. Tobias
Department of Chemical Engineering
and Lawrence Berkeley Laboratory
University of California
Berkeley, CA 94720

Introduction

Electrolytic gas evolution has been recognized in the literature since 1951 (Roald and Beck, 1951) as an efficient means of achieving high mass-transfer rates at solid surfaces. The magnitude of this effect can be illustrated by comparing the equivalent diffusion boundary-layer thicknesses for gas evolution and for forced convection. Ibl et al. (1971) measured mass-transfer rates during electrolysis by adding Fe^{+3} to the electrolyte as an indicator ion: the Fe^{+3} is reduced at limiting current simultaneously as the hydrogen ion is discharged. For hydrogen evolution at a planar vertical surface at a rate of 1 $cm^3/cm^2 \cdot min$, which corresponds to a current density of 130 mA/cm^2, they determined a diffusion-layer thickness δ of 15 μm, or a mass-transfer coefficient k of 3.6×10^{-3} cm/s. For comparison, we calculate the average diffusion boundary-layer thickness for developed mass transfer in turbulent channel flow with the correlation of Landau and Tobias (1976)

$$Sh \equiv \frac{d}{\delta} = 0.0113 Re^{0.87} Sc^{0.35} \quad 2{,}800 < Re < 12{,}000 \quad (1)$$

where d is the equivalent diameter, $Re \equiv ud/v$, and $Sc \equiv v/D_i$. For a Sc of 1,800, the Re required to obtain the average diffusion boundary layer thickness of 15 μm is 6,700. In a 1-cm square channel, the equivalent diameter d is 0.5 cm and the required average velocity between parallel plate electrodes is 135 cm/s. Thus gas evolution indeed provides a very effective stirring mechanism.

The reason gas evolution is so effective a stirring mechanism is that the bubble motion takes place in the near vicinity of the electrode surface, within and just outside the mass-transfer boundary layer. Gas evolution is a very complex process, involving bubble nucleation, growth, coalescence, and detachment from the electrode. In addition to these local events, a macroscopic flow is generated by the rise of bubble swarms or curtains. In practice, forced convection is often superimposed to facilitate removal of the gas from the interelectrode gap, thereby lowering the ohmic penalty for the presence of gas in the electrolyte.

The dominant mechanism for the high mass-transfer enhancement by gas evolution is not obvious. In fact, it may be different under different conditions of gas-evolution rate, and electrode coverage, orientation, or morphology. The traditional approach has been to assume a primary mode of mass transfer, quantify the mass transfer rate for the chosen mode, and average over the electrode area to obtain a relation between the mass-transfer rate and the gas-evolution rate. An example of this approach would be the application of the penetration or surface-renewal model, according to which the important mechanism of mass transfer is diffusion to the newly-exposed electrode site following each bubble disengagement. Several schools of thought have emerged over the past two decades, each emphasizing a different mechanism as the main contributor; these will be briefly reviewed in the following section. The reader is

The present address of G. M. Whitney is IBM Corporation, 5600 Cottle Road, San Jose, CA 95193.

referred to recently published reviews (Vogt, 1983; Sides, 1986) for details on various other aspects of electrolytic gas evolution.

Recent advances in integrated-circuit processing have allowed the limiting-current technique of measuring mass-transfer coefficients to be applied at electrodes that are sectioned on the microscopic scale. The first study of this type involving gas-evolving electrodes by Dees and Tobias (1987b) resolved on a scale of 100 μm the mass transfer resulting from a single bubble detaching from a *horizontal* electrode, and also that resulting from two bubbles coalescing and rising from the electrode. They found that *the mass transfer following a coalescence event was significantly more intense than that following a single disengagement.* A coalescence and simultaneous disengagement increased the mass-transfer rate by an order of magnitude over the free-convection limiting current, while a single-bubble disengagement increased the mass-transfer rate by only a few percent.

The objective of the present work is to resolve spatially and temporally the mass transfer resulting from a *single* stream of gas bubbles evolved at or near a *vertical* micromosaic electrode. Our aim is to characterize the nature of the enhancement in an effort to fill in the missing microscopic picture, so that the correlation of mass-transfer enhancement data, and ultimately, the engineering design of gas-evolving electrodes, may be based on the fundamental physicochemical principles. The specific topic addressed in this study is the dependence of the magnitude and spatial distribution of the mass-transfer enhancement at vertical gas-evolving electrodes on bubble size, bubble stream position relative to the mass-transfer surface, and rate of gas evolution.

Models for Mass-Transfer Enhancement

Three theories of mass transfer at gas-evolving electrodes have been advanced, each emphasizing a particular mechanism of mass-transfer enhancement. These theories are the penetration model, the hydrodynamic model, and the microconvection model.

Penetration model

The penetration model, or surface-renewal effect, was first proposed by Higbie (1935) in relation to the absorption of a gas into a liquid, and was adopted by Ibl and coworkers (Ibl and Venczel, 1970) for electrolytic gas evolution. In this description, a volume of fluid in the mass-transfer boundary layer, having been depleted of reactant, is renewed as each bubble detaches from the electrode and allows fresh electrolyte with bulk concentration of reactant to penetrate to the electrode. The transport of reactive species to the nucleation site at the electrode is by diffusion during a waiting period τ_w before a new bubble is nucleated. The reactant-ion limiting current during the waiting time falls with $t^{-1/2}$ following the Cottrell (1903) equation,

$$i(t) = \frac{n_i F D_i c_i^\infty}{\sqrt{\pi D_i t}} \tag{2}$$

The average limiting current during the waiting time is

$$i = \frac{1}{\tau_w}\int_0^{\tau_w} i(t)\,dt = \frac{2n_i F D_i c_i^\infty}{\sqrt{\pi D_i \tau_w}} \tag{3}$$

If one assumes that the bubble growth time is insignificant in comparison to the total life-cycle time, the waiting time τ_w is inversely proportional to the bubble frequency and hence to the volumetric flux of evolved gas. In this case, i and the mass-transfer coefficient k will depend on v, the volumetric rate of gas evolution per unit area, to the $\frac{1}{2}$ power. The constant of proportionality is subject to various assumptions involving electrode coverage and the shape of attached bubbles. Ibl and Venczel (1970) assumed that bubbles adhering to the electrode were hemispherical in shape, covering an area of πR_b^2. The waiting time was then the ratio of the gas volume per bubble to the product of the gas evolution rate v per electrode area and the area per bubble, πR_b^2.

$$\tau_w = \frac{2\pi R_b^3}{3v\pi R_b^2} = \frac{2R_b}{3v} \tag{4}$$

To account for the fact that, on the average, a fraction θ of the electrode is blocked by attached bubbles, Ibl and Venczel multiplied τ_w and k by $1 - \theta$. Substituting Eq. 4 into Eq. 3, they obtained

$$i = n_i F c_i^\infty \left[\frac{6D_i v(1-\theta)}{\pi R_b}\right]^{0.5} \tag{5}$$

Experimentally determined values of $\partial \ln k/\partial \ln v$ fall between 0.3 and 0.7. A summary is listed in Table 1.

Hydrodynamic model

The second theory of mass-transfer enhancement at gas-evolving electrodes is the hydrodynamic model, first proposed in relation to nucleate boiling by Zuber (1963). The model was discussed in relation to gas evolution by Janssen and Hoogland (1970, 1973) and described quantitatively by Janssen and Bar-

Table 1. Experimentally Determined Values of $\partial \ln k/\partial \ln v$ (Vogt, 1983)

Gas	Electrolyte	$\partial \ln k/\partial \ln v$	Investigator
H_2	Alkaline	0.43	Green & Robinson (1959)
		0.29	Vondrak & Balej (1970)
		0.36	Janssen & Hoogland (1973)
		0.25	Fouad & Sedahmed (1973)
		0.65	Rousar *et al.* (1975)
		0.17–0.30	Janssen (1978)
H_2	Acidic	0.5(0.59)	Roald & Beck (1951)
		0.525	Venczel (1961)
		0.47	Janssen & Hoogland (1970)
		0.62(Pt)	Janssen & Hoogland (1973)
		0.36(Hg)	Janssen & Hoogland (1973)
		0.45	Kind (1975)
		0.15($i < 80$ mA/cm^2)	Alkire & Lu (1979)
		0.53($i > 80$ mA/cm^2)	Alkire & Lu (1979)
O_2	Alkaline	0.87/0.33	Janssen & Hoogland (1973)
		0.4	Fouad & Sedahmed (1973)
O_2	Acidic	0.5	Beck (1969)
		0.4	Janssen & Hoogland (1970)
		0.6	Ibl *et al.* (1971)
		0.57	Janssen & Hoogland (1973)
		0.66	Kind (1975)
Cl_2	Acidic	0.71	Janssen & Hoogland (1970)

endrecht (1979). This treatment emphasizes the electrolyte flow caused by the buoyant lift of the rising bubbles in the vicinity of the electrode. The mass-transfer correlation for turbulent natural convection at a plane wall,

$$Sh_H \equiv \frac{kH}{D_i} = 0.16(GrSc)^{1/3} \tag{6}$$

is assumed to be applicable to the case of two-phase flow. The Grashof number Gr is defined

$$Gr \equiv \frac{gH^3}{\nu^2}\frac{\rho^\infty - \rho^0}{\rho^0} \tag{7}$$

where ρ^∞ is the density of the bulk solution, and ρ^0 is the mean density at the electrode surface. The bulk density ρ^∞ is equal to the density of the liquid ρ_L, and ρ^0 is a function of the gas volume fraction ϵ: $\rho^0 = \epsilon\rho_G + (1 - \epsilon)\rho_L$. For $\rho_L \gg \rho_G$, the Grashof number becomes

$$Gr = \frac{gH^3}{\nu^2}\frac{\epsilon}{1 - \epsilon} \tag{8}$$

Zuber (1963) related the volume fraction to the volumetric rate of gas evolution per unit area by

$$\frac{\epsilon}{1 - \epsilon} = \frac{v}{v_t} \tag{9}$$

where v_t is the terminal velocity of a single bubble and, for a small spherical bubble with a rigid interface, is given by

$$v_t = \frac{1}{12}\frac{gd^2}{\nu}\frac{\rho_L - \rho_G}{\rho_L} \tag{10}$$

Equation 9 is valid in the turbulent regime, in which a net upward flow is induced by the rising bubbles. If the liquid were stationary, Eq. 9 would be replaced by

$$v = \epsilon v_t \tag{11}$$

Similarly, if the net upward flow were zero, so that liquid flowed downward to replace the ascending gas, one would obtain the "laminar" result of Zuber (1963)

$$v = v_t\epsilon(1 - \epsilon) \tag{12}$$

In any case, gas volume fractions are typically small compared to unity, so that $\epsilon/(1 - \epsilon)$ in Eq. 8 may be replaced by v/v_t. Substituting this result and Eqs. 8 and 10 into Eq. 6, one obtains

$$Sh \equiv \frac{kd}{D_i} = 0.16\left(\frac{12\rho_L}{\rho_L - \rho_G}\right)^{1/3}\left(\frac{vd}{D_i}\right)^{1/3} = 0.37(ReSc)^{1/3} \tag{13}$$

The mass-transfer rate is proportional to the gas-evolution rate to the 1/3 power. This result may be applicable to gas evolution under certain conditions of current density and electrode coverage. Ibl et al. (1971) experimentally determined the slope of the ln k vs. ln v curve to be 0.36 for gas-sparged systems. Economou and Alkire (1985) also obtained 0.36 as the exponent for gas-sparged systems with superimposed liquid flow.

Microconvection Model

The microconvection model was developed by Vogt (1977) and Stephan and Vogt (1979). Their approach treats the mass transfer caused by the local convection generated by the growth of an attached bubble. The electrode area per bubble available for mass transfer is $1/(n/A) - \pi R_b^2$, where R_b is a function of time. The local, transient mass transfer for laminar flow is averaged over this area and over the time of bubble growth. In the resulting correlation,

$$Sh = 0.93Re^{0.5}Sc^{0.487} \tag{14}$$

Sh is a factor of approximately two below that calculated from the penetration model.

The important point to be gained from these mass-transfer theories is that single-bubble disturbances of the mass-transfer boundary layer, such as those emphasized in the penetration and the microconvection models, result in a dependence of the mass-transfer coefficient on the gas-evolution rate to the 1/2 power. The mass-transfer enhancement resulting from macroconvection generated by the buoyant lift of bubble swarms depends on the gas evolution rate to the 1/3 power.

Experimental Method

The micromosaic electrode used in this study was conceived by Dees and Tobias (1982) and was designed in a collaborative effort with the Hewlett-Packard Company. The design was modified for this investigation, and the electrodes were fabricated using integrated-circuit technology at Hewlett-Packard Laboratories, and later at AT&T Bell Laboratories. The electrode is fabricated on a 7.62 cm silicon wafer. The active area, shown in Figure 1, consists of a 5 mm platinum square. The center 1 mm square of the active area comprises a 10 × 10 array of 96 μm square platinum segments on 100 μm centers; the remaining part of the active area acts as a buffer segment to eliminate edge effects in the center region. In addition, there are

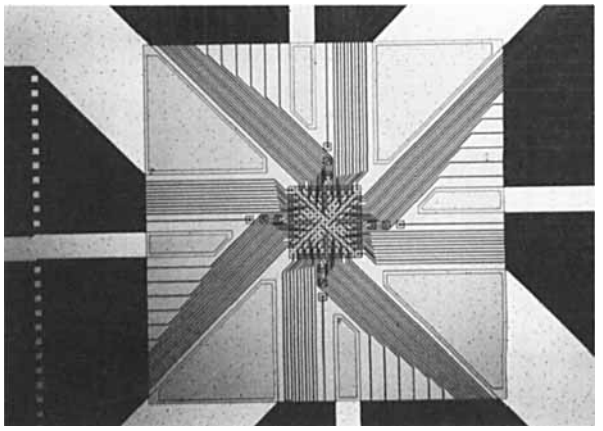

Figure 1. Center 5 mm active area of micromosaic electrode.
Segmented area and surrounding buffer section are included

twelve satellite segments positioned within the buffer segment at distances of 100, 300, and 500 μm from the segmented area. An enlargement of the center section is shown in Figure 2. The segmented area of the electrode and the buffer and satellite segments together make up the working electrode, which simulates a continuous surface but contains many electrically-isolated electrode elements.

The micromosaic electrode is housed in a Plexiglas cell along with two platinum counterelectrodes and a reference-electrode capillary. A printed-circuit board presses onto the electrode edges to bring out the electrical connections. An O-ring seal between the cell body and the wafer ensures leak-free containment of the electrolyte. A data acquisition system developed by Dees (1983) includes current-to-voltage converters for each of the 112 segments, and a Multiplexer channel scanner which can monitor the current to each of the electrode segments at rates from 1.25 to 10.0 kHz. The data are taken by a Hewlett-Packard 9825T desktop computer, stored on floppy disk, and later transferred to a mainframe computer. Dees and Tobias (1982, 1987a) give a detailed description of the fabrication of the first generation of electrodes and of the data acquisition system. Modifications of electrode fabrication and the materials used in the electrodes built for this study are described elsewhere (Whitney, 1987).

The limiting-current technique is used to monitor the rate of mass transfer to the surface. The working electrode potential is held at 500 mV cathodic to a mercury/mercurous sulfate reference electrode. At this potential, the reduction of the indicator ion Fe^{+3} to Fe^{+2} from 0.0484 M $Fe_2(SO_4)_3$ in 0.5 M H_2SO_4 proceeds at a rate that is indicative of the prevailing mass-transport conditions.

The mass-transfer disturbance is produced, as well as monitored, electrochemically. A bubble stream is generated at one of the satellite segments in the plane of the micromosaic electrode by making the potential at that segment several hundred milivolts more cathodic than the rest of the electrode. The satellite segments were used for all of the experiments in which the bubble stream was rising within the mass-transfer boundary layer.

The experiments in which the bubble stream was generated away from the electrode surface were conducted using a modified cell top, shown in Figure 3. A post extending through the top of the cell (lower right in photo) holds a platinum wire electrode whose position with respect to the micromosaic electrode can be adjusted by turning the teflon nut. A Brown and Sharpe dial gauge (lower left) rests on top of the post and allows the measurement of position of the wire electrode with respect to the micromosaic to within about 12 μm. The completely-assembled cell is shown in Figure 4.

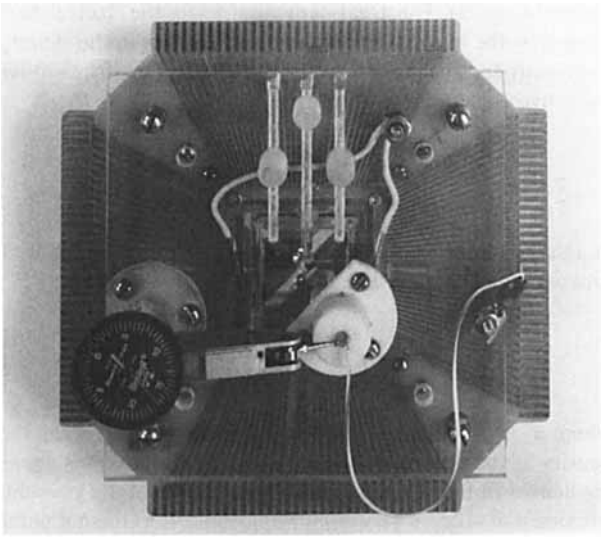

Figure 3. Closeup of assembled cell holding micromosaic electrode.
Dial gauge (lower left) measures position of bubble-generating electrode relative to micromosaic electrode

The possibility of dissolved hydrogen being oxidized at the electrode and obscuring the mass-transfer measurement was quantified by performing experiments in 0.5 M H_2SO_4, with no indicator ion added to the electrolyte. For a 30 μA bubble stream generated at the satellite segment 500 μm below the square array of monitoring segments, the average hydrogen oxidation current to the segmented area was 0.16 mA/cm^2. This represents a possible source of error of about 3%. In all experiments in which the bubble stream was generated in the plane of the micromosaic the lowest of the satellite segments was used to minimize this possible error. Further details are provided by Whitney (1987).

Bubble size was determined by estimates from still photo-

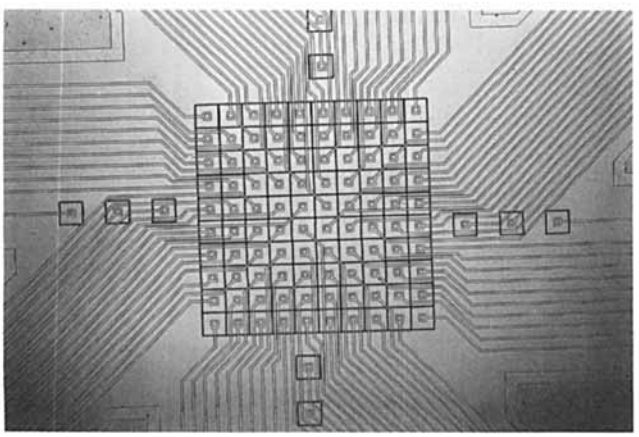

Figure 2. Center segmented portion, 1 mm square, of micromosaic electrode.

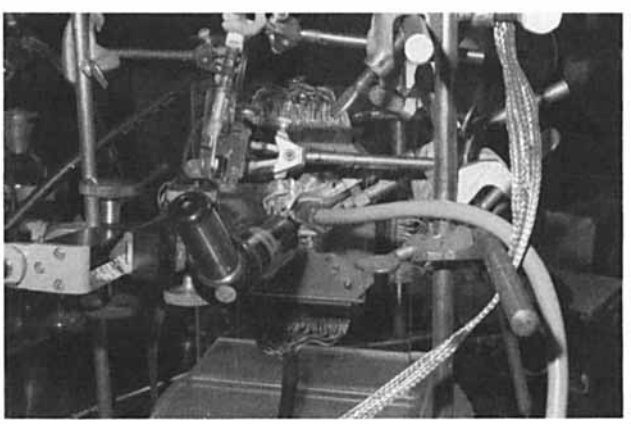

Figure 4. Experimental apparatus for vertical gas evolution experiments.

graphs taken through a microscope and using the micromosaic electrode itself as the scale. The determination of the distance of separation between the electrode and bubble streams generated within the mass transfer boundary layer was accomplished using high-speed cinematography with a modified electrode, in a special cell. A micromosaic electrode was cut, and the center section mounted onto a Plexiglas strip that fits on one side of a prismatic viewing cell. Contacts from the bonding pads at the edge of the electrode were connected with conductive silver epoxy to screws in the Plexiglas. One of the connected segments was used to generate a stream of hydrogen bubbles, and the other segments and the buffer section were polarized as they would be in a mass-transfer experiment. The stream of rising bubbles was filmed at 720 frames/s with a Redlake Corporation Hycam Model 41-0004 16 mm camera.

Results

The modes of mass-transfer enhancement observed for the case of the bubbles rising *within* the mass-transfer boundary layer and for the case of the bubbles rising *outside* the mass-transfer boundary layer are qualitatively distinct and lend themselves to different analyses. The results and analyses for the two cases are presented separately.

Bubbles rising within the mass-transfer boundary layer

Bubbles generated in the plane of the micromosaic electrode surface at one of the satellite segments below the 10 × 10 array of monitoring electrodes are typically 45 to 100 μm in diameter at the time of detachment. High-speed cinematography revealed that upon leaving the growth site, a bubble slides along the electrode for a distance corresponding to several bubble diameters, and then separates from the electrode and rises at a constant separation of approximately one bubble radius. Thus the bubbles rise entirely within the free-convection mass-transfer boundary layer (approximately 150 μm in thickness), established by the indicator-ion reaction. Figure 5 is taken from a high-speed movie of H_2 evolution in the viewing cell described above. The detached bubbles are 100 μm in diameter. The smallest bubble, approximately 30 μm in diameter, is still attached at the growth site. The bubble immediately above it is sliding along the electrode, and the uppermost bubble is rising at a separation of roughly 30 μm.

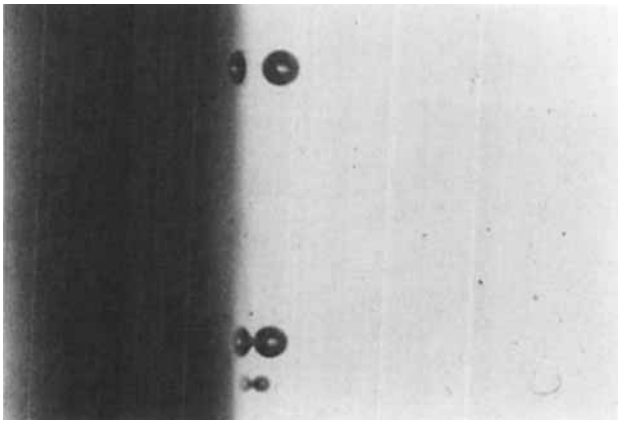

Figure 5. Bubbles rising along micromosaic strip electrode.
High-speed movie frame 1.4 mm wide × 1.1 mm high

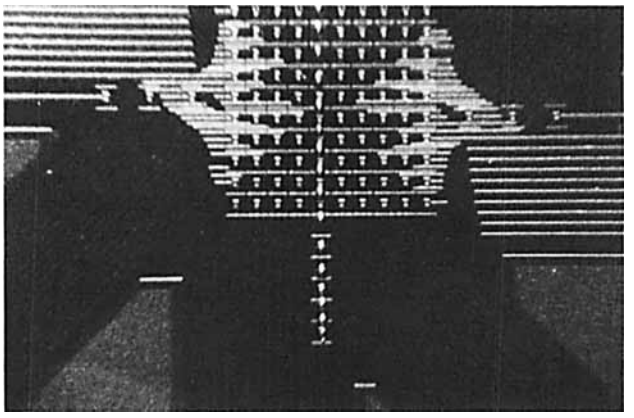

Figure 6. Photograph taken during mass transfer experiment: 60 μm dia. bubbles rising along micromosaic electrode.
Bubble stream generated at 8.5 μA rate from site 500 μm below array of monitoring electrodes

Figure 6 is a photograph taken during an experiment that uses the entire micromosaic electrode. A stream of 60 μm dia. bubbles is generated by an 8.5 μA current at the lowest of the satellite segments below the array of monitoring electrodes. Figure 7 shows the current response of one of the monitoring segments directly in the path of the bubble stream. Time zero is the start of data acquisition; the transport processes are presumably in a steady, possibly periodic, state before this. The currents to two segments located at the same height, but 100 and 500 μm to the side, respectively, are also shown. One can see that the average mass-transfer rate to the segments close to the bubble path is enhanced by a factor of approximately 1.5. The frequency of the oscillations corresponds to the frequency of bubble evolution. The periodic enhancement of mass transfer is attributed to the bubble passing over the segment and disrupting the boun-

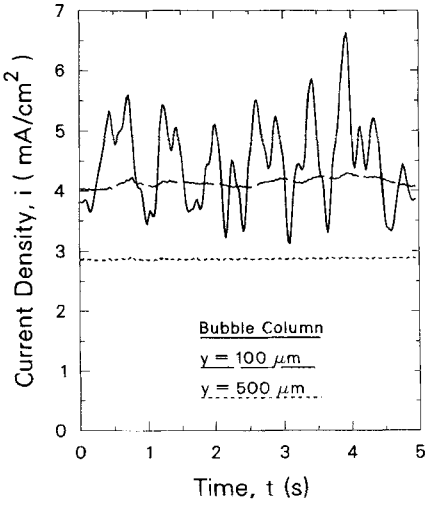

Figure 7. Current to three segments showing effect of 60 μm H_2 bubbles rising within mass transfer boundary layer generated by 8.5 μA current.
Segments are (1) directly in the bubble path; (2) 100 and (3) 500 μm to the side

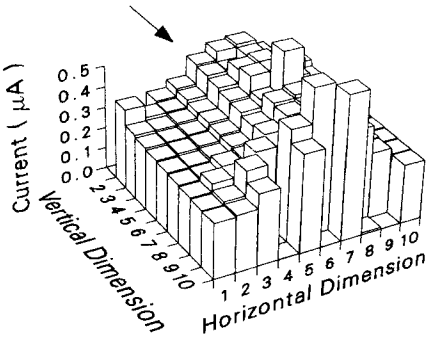

Figure 8. Spatial distribution of mass-transfer rate enhanced by 60 μm H_2 bubbles generated by 8.5 μA current rising within mass transfer boundary layer.

Abruptly higher current densities at some segments (*e.g.*, [10, 5], [10, 7]) caused by nonfunctioning adjacent segments

dary layer. The mass-transfer rate decreases during a diffusion-dominated decay period until the next bubble arrives.

The spatial variation of the mass-transfer enhancement due to the rising bubble streams can be seen by comparing the curves in Figure 7; one can see that at least two columns receive enhanced mass transfer due to the rising bubbles. The edge column is unaffected by the bubble stream. Figure 8 shows the spatial distribution of mass-transfer rate for the matrix of monitoring electrodes averaged over the 5 s duration of the run. The site of bubble evolution is behind the monitoring electrodes in the figure and the bubbles rise toward the viewer, as indicated by the arrow. Figures 7 and 8 show that the mass-transfer enhancement is fairly localized, affecting an area of approximately four columns, or seven bubble diameters, in width. The end columns are unaffected by the rising bubbles; the current to the end columns is approximately 0.25 μA per segment, which corresponds to 2.5 mA/cm^2 or a mass-transfer coefficient of 2.5×10^{-4} cm/s. This is the value of the background natural-convection current, generated by the redox reaction itself.

An example showing the magnitude of the mass-transfer effect is given in Figure 9, in which the current to one segment from the column closest to the bubble path is plotted as a function of time for several experiments with different bubble evolution rates. As expected, the mass-transfer rate increases with the bubble-evolution frequency. A plot of the current distributions across the segmented portion of the electrode for bubble evolution rates of 3.5 and 8.5 μA are shown in Figure 10. As the bubble evolution rate is increased, the mass-transfer rate to the segments within 200 μm of the bubble path is increased, but the current to the edge columns remains unaffected at the value of the background natural-convection current. As will be seen in the next section, these results are in good agreement with those provided by the surface-renewal theory of mass-transfer enhancement.

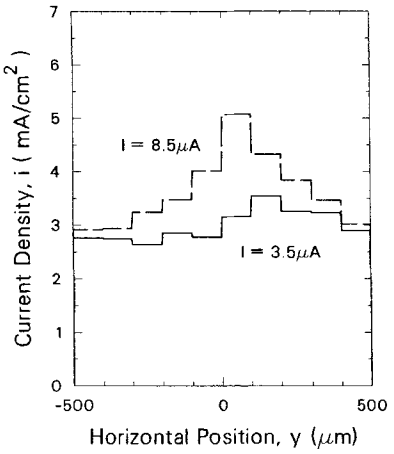

Figure 10. Distribution across electrode of mass transfer rate enhanced by 50 μm H_2 bubbles rising within mass-transfer boundary layer.

Bubbles rising outside the mass-transfer boundary layer

For the case of bubbles rising outside the mass-transfer boundary layer, the transient response of the monitoring electrodes is much more steady in time than for the case of bubbles rising very close to the electrode. Figure 11 shows the transient mass transfer to one segment, again closest to the path of the rising bubble stream, as a result of 30 μA bubble streams rising 200, 300, and 450 μm away from the electrode. One can see that

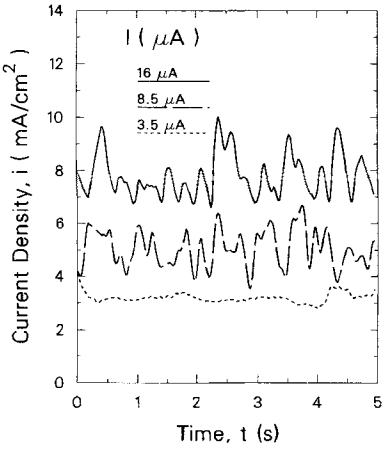

Figure 9. Transient mass transfer to a segment in column closest to bubble stream for three bubble evolution rates, *I*.

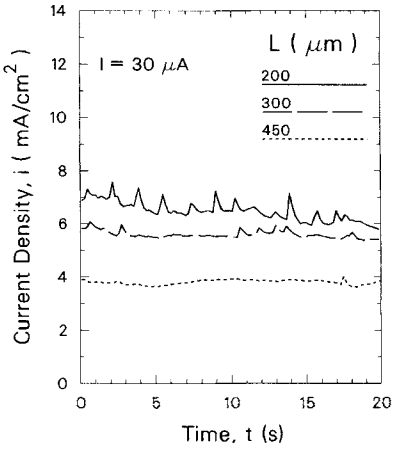

Figure 11. Transient mass transfer to a segment in column directly behind bubble stream.

L, bubble stream position

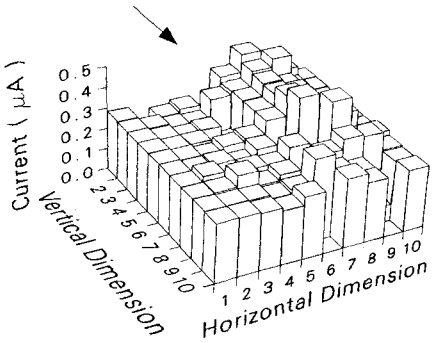

Figure 12. Spatial distribution of mass-transfer rate enhanced by 100 μm H_2 bubbles generated by 30 μA current 750 μm from electrode surface.

the magnitude of the mass-transfer enhancement is strongly dependent on bubble-stream position. The oscillations in the mass-transfer rate due to the passing of individual bubbles are virtually absent when the bubble stream is 300 μm from the electrode or beyond.

Figure 12 shows the time-averaged mass-transfer distribution for an experiment in which the distance between the bubble evolution site and the electrode is 750 μm. The magnitude of the enhanced mass transfer decreases with increasing distance from the electrode. Note, however, that the currents to the edge columns are considerably higher than the background natural-convection current of 0.25 μA. The enhancement from bubble streams rising outside the mass-transfer boundary layer is significant, steady, and less localized than that from bubble streams rising within the mass-transfer boundary layer.

Analysis and Discussion

Bubbles rising within the mass-transfer boundary layer

Bubble streams rising within the mass-transfer boundary layer result in fluctuating, localized mass-transfer enhancement to the electrode surface. In light of this, we wish to examine our results in the context of a surface-renewal theory of mass-transfer enhancement. We first present a general derivation for surface renewal at vertical gas-evolving electrodes, and then consider the special case of a single bubble stream originating from one position on the electrode.

Surface Renewal at Vertical Gas-Evolving Electrodes. Consider streams of bubbles of radius R_b rising upward along the electrode surface and sweeping a renewal path of width $2R_b$. From the time a bubble crosses a horizontal line at vertical position z, until the next bubble arrives, the current density at z falls according to the Cottrell (1903) equation for transient one-dimensional diffusion in a stagnant medium,

$$N = c_i^\infty \sqrt{\frac{D_i}{\pi t}} \tag{15}$$

The average flux over the surface of the electrode is N averaged over the electrode area and over the time between surface renewals. We will follow the description by Danckwerts (1951) in considering a distribution of surface ages. Let $\phi(t)dt$ be the fraction of surface area that is of a surface age, or time since last being renewed, between t and $t + dt$. Let s be the mean rate of fractional surface renewal, assumed constant in time, but possibly a function of position. The fraction of surface with surface age between t and $t + dt$ is equal to that with surface age between $t - dt$ and t minus the fraction renewed in time dt.

$$\phi(t)dt = \phi(t - dt)dt - \phi(t - dt)dt \cdot sdt \tag{16}$$

Dividing by dt and taking the limit as $dt \to 0$ gives

$$\frac{d\phi}{dt} = -s\phi \tag{17}$$

Integrating Eq. 17 with the conditino that $\int_0^\infty \phi(t)\,dt = 1$ gives

$$\phi(t) = se^{-st} \tag{18}$$

The average flux over time is the integral of the transient flux times the fraction of surface with surface age t.

$$\bar{N} = c_i^\infty \int_0^\infty \sqrt{\frac{D_i}{\pi t}}\, se^{-st}\, dt \tag{19}$$

For the case of gas evolution at a vertical electrode, the mean rate of surface renewal by bubbles rising along the electrode is a function of vertical position z on the electrode. The flux to the electrode must be averaged over electrode height z from 0 to H. The fraction of surface area at z that is renewed per unit time is equal to the rate at which bubbles cross a horizontal line of length w at height z, times the probability that any given point on the line is in the renewal path.

$$s(z) = \dot{n}_z \frac{2R_b}{w} \tag{20}$$

where R_b is the bubble radius and $2R_b$ is the renewal path width. $\dot{n}_z$ is the total bubble evolution rate, in bubbles released per second, below height z and, assuming the volumetric gas evolution rate v to be uniform, is given by

$$\dot{n}_z = \frac{v}{4/3\pi R_b^3} wz \tag{21}$$

Equation 19 integrated over time is

$$\bar{N} = \frac{c_i^\infty \sqrt{D_i}}{H} \int_0^H \sqrt{s(z)}\, dz \tag{22}$$

If s were independent of z, we would obtain the result of Danckwerts (1951)

$$\bar{N} = c_i^\infty \sqrt{D_i s} \tag{23}$$

Inserting Eqs. 20 and 21 into Eq. 22 and integrating, we finally obtain

$$\bar{N} = c_i^\infty \int_0^\infty \sqrt{\frac{2D_i v H}{3\pi R_b^2}} \tag{24}$$

We would expect the above description to have validity only at low current densities, where flow of the bulk fluid does not

become appreciable. Fouad and Sedahmed (1972) found that the mass-transfer rate increases with increasing electrode height for low current densities (2 to 10 mA/cm^2) of hydrogen evolution over the entire range of electrode heights investigated (2.5 to 50 cm), though not as strongly as a square root dependence. For higher current densities of hydrogen evolution (15 to 40 mA/cm^2), the mass-transfer rate *decreases* with increasing electrode height for the shorter electrodes (2.5 to 10 cm). For oxygen evolution, the mass-transfer rate increases with increasing electrode height, in this case for the entire range of electrode heights and current densities investigated (2.5 to 50 cm, and 2 to 60 mA/cm^2). Janssen and Hoogland (1970) found the opposite trend to hold for oxygen evolution at vertical electrodes of height 0.3 to 2 cm and at current densities of 10 to 400 mA/cm^2, the mass transfer coefficient falling with electrode height to the -0.13 power.

The observed decrease of mass-transfer rate with height at short electrodes may be simply due to the increasing diffusion boundary-layer thickness with height as given by boundary-layer theory. For the higher current densities, the increase in mass transfer with increasing height will undoubtedly be aided by bulk convection, which was not accounted for in the above treatment. We simply note at this point that the surface-renewal theory based on bubbles sweeping a path as they slide along the electrode gives the same value (½) of the exponent on the gas-evolution rate v as the other surface-renewal theories.

Surface Renewal with a Single Bubble Stream. The surface-renewal theory applied to the results described in the previous section is simpler than presented above in that we do not have a random distribution of surface ages. The bubble stream rises along the electrode surface on a particular path and sweeps a region of width $2R_b$ with a frequency equal to the bubble evolution frequency, $3\dot{V}/4\pi R_b^3$, where $\dot{V}$ is the volumetric rate of gas evolved. Substituting the bubble evolution frequency for $1/\tau_w$ in the integrated form of Eq. 15, we obtain the average flux $\overline{N}_\tau$ to the area being renewed:

$$\overline{N}_\tau = 2c_i^\infty \sqrt{\frac{3D_i\dot{V}}{4\pi^2 R_b^3}} \tag{25}$$

The area that is periodically renewed is $2R_bH$. The average flux to an area wH is then

$$\overline{N}_{\tau,A} = \overline{N}_\tau \frac{2R_bH}{wH} = c_i^\infty \sqrt{\frac{12D_i\dot{V}}{\pi^2 R_b w^2}} \tag{26}$$

The above description does not include a flux contribution from the electrode area lying outside the renewal path. In fact, the rest of the electrode is receiving a flux due solely to the background natural-convection current density i_{nc}. The overall flux to the electrode, expressed as a current density, includes contributions from the renewal area of width $2R_b$ and the nonrenewed area of width $(w - 2R_b)$.

$$i_{avg} = [i_{nc}(w - 2R_b) + n_iF\overline{N}_\tau 2R_b]/w \tag{27}$$

$$i_{avg} = i_{nc} + \left(\frac{n_iFc_i^\infty}{\pi}\sqrt{\frac{12D_iRTI}{n_gFpR_b}} - 2R_bi_{nc}\right)\frac{1}{w} \tag{28}$$

The ideal gas law has been used to relate $\dot{V}$, the volumetric rate of gas evolution, to I, the current passed to generate the bubble stream, and n_g, the number of electrons transferred in the gas evolution reaction, assuming all the hydrogen produced is captured by the bubble. A nonunity capture efficiency will be included in the effective bubble radius. Equation 28 is valid for electrode width w greater than the renewal path $2R_b$. With the micromosaic electrode we can conveniently vary w by varying the number of columns of segments over which we average the mass-transfer rate. We can, in effect, vary the electrode width by simply grouping the data from the same experiment in different ways. If we plot the average current density as a function of $1/w$, where w is the electrode width over which we average, we should obtain a straight line with a slope of

$$b = \frac{n_iFc_i^\infty}{\pi}\sqrt{\frac{12D_iRTI}{n_gFpR_b}} - 2R_bi_{nc} \tag{29}$$

and a y intercept of i_{nc}. Knowing b, i_{nc}, and I, the current to generate the bubble stream, we can solve Eq. 29 for R_b, the effective bubble radius.

If $w < 2R_b$, Eq. 28 is no longer valid; the average current becomes equal to the renewal current, $n_iF\overline{N}_\tau$, where $\overline{N}_\tau$ is given by Eq. 25. Knowing R_b, we can calculate i_{max}, the renewal current. Thus using the slope and the y intercept from the part of the curve for small $1/w$, we can calculate the limiting value of the curve as $1/w$ becomes large with respect to $1/(2R_b)$.

Figure 13 is the plot of the average current density vs. $1/w$ for two experiments, in which the bubble evolution rates were 3.5 and 8.5 μA, respectively. The current distribution plots for these two runs appear in Figure 10. For small $1/w$, the points lie on a straight line. The y intercept of approximately 2.8 mA/cm^2 corresponds to the background natural convection current measured independently. There is a region of transition from approximately 25 to 50 cm^{-1}, beyond which the current density reaches a plateau. The effective bubble radii from Eq. 29 for the two runs were found to be 160 and 170 μm, factors of 6.4 and 5.7 greater than visual estimates from photographs, such as the one shown in Figure 8 for the 8.5 μA run. Values of I and R_b were

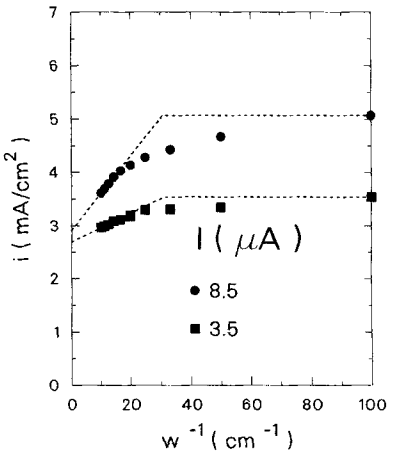

Figure 13. Enhanced mass transfer rate vs. inverse of averaging width w for two experiments.

Upper curve: 60 μm H_2 bubble stream evolved at 8.5 μA rate within mass transfer boundary layer.
Lower curve: 50 μm H_2 bubble stream evolved at 3.5 μA rate

Table 2. Effective Bubble Radii and Renewal Currents from Eqs. 29 and 25

I μA	R_b μm	i_{nc} mA/cm²	$10^2 b$ mA/cm	$R_{b,eff}$ μm	Eff. factor	i_{max}^{exp} mA/cm²	i_{max}^{calc} mA/cm²	Δ %
3.5	25	2.69	2.73	160	6.4	3.54	3.54	0.0
4.5	22	2.51	4.88	159	7.2	4.06	4.04	0.4
8.5	30	2.91	7.01	172	5.7	5.07	4.95	2.4
9.0	22	2.82	8.67	164	7.5	5.66	5.46	3.5
16.0	38	2.71	8.93	218	5.7	5.46	4.76	12.8

inserted into Eq. 25 to calculate the maximum current density for $1/w > \frac{1}{2}R_b$. These values were found to agree within several percent with the experimentally measured values of the current to the 100 μm wide column of electrodes in the bubble path. These are the values plotted in Figure 13 for 100 cm^{-1}.

Table 2 summarizes the application of the surface-renewal theory to a series of five experiments in which the bubble stream rises within the mass-transfer boundary layer. The effective bubble radius varies from 5.7 to 7.5 times the experimentally-determined bubble radius. This factor is not surprising when one considers the spatial distribution of the mass-transfer rate. Figure 14 shows this distribution averaged along the height of the electrode for one of the runs described above. The visually observed bubble diameter for this experiment is 60 μm, while the effective bubble diameter was found to be 340 μm. From Figure 14, we can see that the path of enhanced mass transfer is appreciably wider than the actual bubble diameter. In the simplified theory described here, we consider the actual distribution shown in Figure 14 to be idealized as having only two possible values, as shown by the dashed curve: the value of the current to the renewal path is i_{max} and that to the rest of the electrode is i_{nc}. The width of the renewal path and the values of i_{max} and i_{nc} were taken from the low $1/w$ values; these are found to match i_{nc} measured in independent experiments, and also i_{max} for large $1/w$ values. Thus the effectiveness factor of 6 to 7.5 is a physically meaningful quantity, representing the width of the renewal path

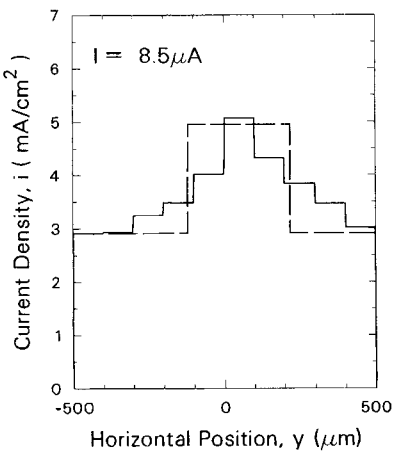

Figure 14. Mass transfer distribution across electrode produced by 60 μm H_2 bubbles rising within mass transfer boundary layer at 8.5 μA rate.

—Measured; --- idealized
Width of renewal path 340 μm; effectiveness factor 5.7

for a bubble stream rising within the mass-transfer boundary layer.

Bubbles rising outside the mass-transfer boundary layer

When the bubble stream rises outside of the boundary layer, the mass-transfer rate is nearly constant in time, the transient effects of individual bubbles being averaged out. Thus the mass-tranfer rate to the electrode reflects only the average effect of the actual pulsating flow caused by successive bubbles.

The treatment that follows is an analysis of the mass transfer induced by the steady rise of a column of ascending bubbles and entrained fluid. The total mass transfer is treated as the combination of that due to the rising cylinder and that resulting from the background natural convection. We first address how to eliminate the natural convection contribution to the total mass-transfer rate.

Background Natural Convection and Assisting Flows. The redox reaction itself causes a density difference between the fluid at the electrode surface and the bulk fluid, the fluid near the electrode being less dense than that of the bulk. This phenomenon is the result of the multicomponent diffusion and migration of ionic species in concentration and potential gradients and is treated in considerable detail in another paper (Whitney and Tobias, 1987). In the cell geometry used in this study, the less dense fluid generated at the electrode causes an upward laminar flow along the electrode surface, which dissipates beyond the upper edge of the active region on the electrode. Under mass transfer control, in the absence of any bubble generation at the electrode, there is a nonuniform current distribution along the electrode: the local current density is proportional to the distance from the lower edge to the $-\frac{1}{4}$ power.

For the case of assisting laminar flows, Churchill (1977) has shown experimentally, and Ruckenstein and Rajagopalan (1980) have demonstrated using scaling arguments that the cube of the effective mass-transfer coefficient is equal to the sum of the cubes of the component coefficients.

$$k_{tot}^3 = k_1^3 + k_2^3 \tag{30}$$

The mass-transfer coefficient is directly proportional to the current density as $i = n_i F k c_i^\infty$, so the measured current densities combine in the same way. The background natural-convection current density to the area of the 10 × 10 array of monitoring electrodes is measured between gas evolution runs. This value is subtracted from the total mass-transfer rate measured during the gas evolution experiments according to Eq. 30. The resulting mass-transfer rate due solely to the influence of the bubble-stream is presented as a function of bubble evolution rate in Figure 15, and as a function of bubble stream position in Figure 16.

Velocity Field around a Cylinder Rising Parallel to a Wall. The steady nature of the mass-transfer enhancement when the bubble stream is outside the mass-transfer boundary layer suggests an idealization of the bubble stream as a steadily rising column of bubbles and entrained fluid. The mass transfer enhancement in such a case results from an increased velocity gradient in the vicinity of the electrode.

The velocity profile for an infinite cylinder rising parallel to a stationary wall can be derived analytically. In rectangular coordinates, x is the normal distance from the electrode, y is the horizontal distance parallel to the electrode, and z is the vertical

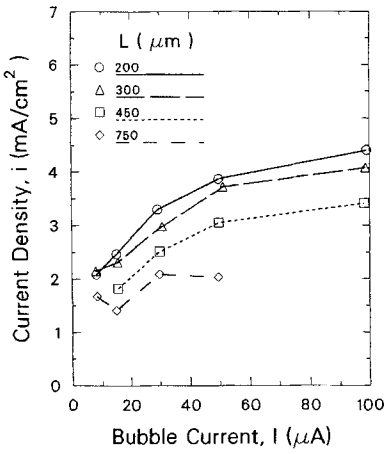

Figure 15. Mass-transfer enhancement as a function of bubble evolution rate.
Averaged over segmented portion of electrode and over time of data acquisition, and corrected for background natural convection current

distance parallel to the electrode and to the axis of the cylinder. The laminar flow problem involves only the z component of velocity. For $v_z(x, y)$, the Navier-Stokes equation reduces to

$$\frac{\partial^2 v_z}{\partial x^2} + \frac{\partial^2 v_z}{\partial y^2} = 0 \tag{31}$$

The solution to Laplace's equation with boundary conditions that the velocity vanishes at the electrode and is equal to the velocity of the cylinder v_c at the surface of the cylinder is

$$v_z = \frac{v_c}{2\eta_c} \ln\left(\frac{x^2 + y^2 + a^2 + 2ax}{x^2 + y^2 + a^2 - 2ax}\right) \tag{32}$$

where

$$a = \sqrt{L^2 - R_c^2} \tag{33}$$

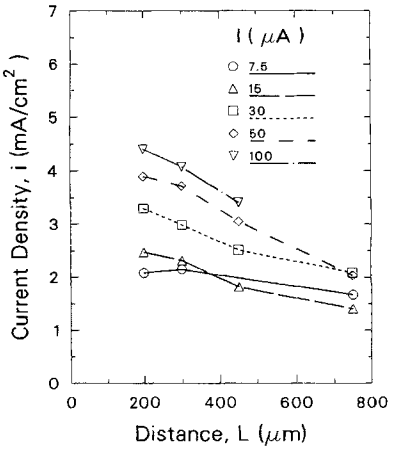

Figure 16. Average mass transfer enhancement to segmented portion of electrode, as a function of bubble stream position.
Corrected for background natural convection current

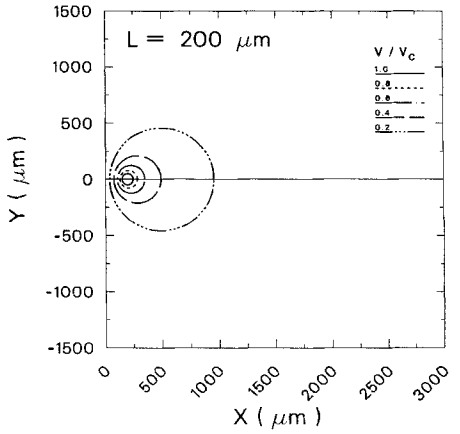

Figure 17. Constant velocity contours for 100 μm dia. cylinder rising at 200 μm from electrode surface.

$$\eta_c = \cosh^{-1}\left(\frac{L}{R_c}\right) = \ln\left[\frac{1}{R_c}(L + \sqrt{L^2 - R_c^2})\right] \tag{34}$$

and L and R_c are the distance from the center of the cylinder to the wall and the cylinder radius, respectively.

The velocity contours from Eq. 32 are shown in Figure 17 for a 100 μm dia. cylinder rising at a center-to-wall distance of 200 μm, and in Figure 18 for a 750 μm distance. Both the velocity gradient and the nonuniformity of the gradient along the electrode surface ($y = -500$ to 500 μm) decrease as the cylinder is moved from 200 to 750 μm. The essence of the idealization of the bubble stream as a rising cylinder can be seen in these two figures; the rising cylinders creates a high velocity gradient at the electrode surface. To obtain the same velocity gradient at the surface by forced convection of the bulk fluid, one would have to maintain fairly high flow rates *of all the fluid in the cell.* The cylinder or bubble stream drags the fluid that is very near the electrode surface upward, producing a high velocity gradient without carrying along a large amount of fluid.

Mass Transfer Aided by a Rising Cylinder. We solve next for the mass-transfer rate to the electrode at $x = 0$ and $z > 0$, by

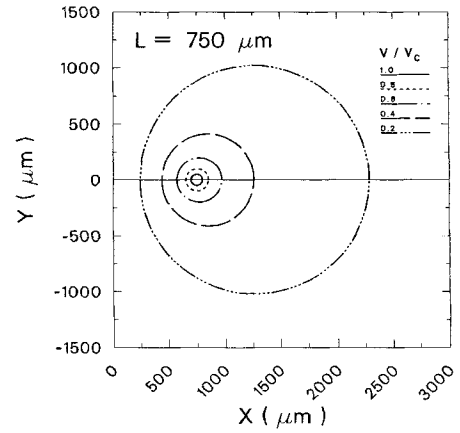

Figure 18. Constant velocity contours for 100-μm dia. cylinder rising at 750 μm from electrode surface.

solving for the gradient of velocity at the wall and inserting this into the equation of convective diffusion:

$$\frac{\partial c_i}{\partial t} + \boldsymbol{v} \cdot \nabla c_i = D_i \nabla^2 c_i \tag{35}$$

The first term is zero at steady state, and the only component of velocity is $v_z(x, y; L, R_c)$. In rectangular coordinates, Eq. 35 becomes

$$v_z \frac{\partial c_i}{\partial z} = D_i \left(\frac{\partial^2 c_i}{\partial x^2} + \frac{\partial^2 c_i}{\partial y^2} + \frac{\partial^2 c_i}{\partial z^2} \right) \tag{36}$$

The boundary conditions are

$$c_i(x = 0, \text{all } y, z > 0) = c_i^0 \tag{37a}$$

$$c_i(x = 0, \text{all } y, z \leq 0) = c_i^\infty \tag{37b}$$

$$c_i(x \rightarrow \infty, \text{all } y, \text{all } z) = c_i^\infty \tag{37c}$$

Diffusion in the y direction may be neglected since the driving force for concentration changes is primarily in the x direction. We make Eq. 36 dimensionless with

$$v_z^* \equiv \frac{v_z}{v_c} \tag{38a}$$

$$\theta_i \equiv \frac{c_i - c_i^0}{c_i^\infty - c_i^0} \tag{38b}$$

and

$$\xi \equiv \frac{x}{a} \tag{38c}$$

Substituting Eqs. 38 into Eq. 36, we obtain

$$\left(\frac{v_c a^2}{D_i} \right) v_z^* \frac{\partial \theta_i}{\partial z} = \frac{\partial^2 \theta_i}{\partial \xi^2} + a^2 \frac{\partial^2 \theta_i}{\partial z^2} \tag{39}$$

The appropriate scaling of z becomes obvious from Eq. 39

$$\zeta \equiv \frac{z}{\frac{v_c a^2}{D_i}} \tag{40}$$

Equation 39 becomes

$$v_z^* \frac{\partial \theta_i}{\partial \zeta} = \frac{\partial^2 \theta_i}{\partial \xi^2} + \left(\frac{D_i}{v_c a} \right)^2 \frac{\partial^2 \theta_i}{\partial \zeta^2} \tag{41}$$

Defining the Peclet number Pe as av_c/D_i we have

$$v_z^* \frac{\partial \theta_i}{\partial \zeta} = \frac{\partial^2 \theta_i}{\partial \xi^2} + \frac{1}{Pe^2} \frac{\partial^2 \theta_i}{\partial \zeta^2} \tag{42}$$

Although the cases we will consider have Re on the order of unity, the Peclet number ($Pe \equiv ReSc$) is high because of the high Schmidt number (~2,000). Thus we can neglect diffusion in the flow direction and solve

$$v_z^* \frac{\partial \theta_i}{\partial \zeta} = \frac{\partial^2 \theta_i}{\partial \xi^2} \tag{43}$$

with boundary conditions

$$\theta_i(\xi = 0, \zeta > 0) = 0 \tag{44a}$$

$$\theta_i(\xi = 0, \zeta \leq 0) = 1 \tag{44b}$$

$$\theta_i(\xi \rightarrow \infty, \text{all } \zeta) = 1 \tag{44c}$$

For small ξ we can approximate v_z as $x \partial v_x/\partial x|_{x=0}$. From Eq. 32

$$\left. \frac{\partial v_z}{\partial x} \right|_{x=0} = \frac{v_c}{\eta_c} \frac{2a}{y^2 + a^2} \tag{45}$$

Substituting Eq. 45 into Eq. 43 and defining $f \equiv y/a$, we obtain

$$\frac{2\xi}{\eta_c (f^2 + 1)} \frac{\partial \theta_i}{\partial \zeta} = \frac{\partial^2 \theta_i}{\partial \xi^2} \tag{46}$$

The similarity variable

$$\lambda \equiv \xi \left(\frac{2}{9\eta_c (f^2 + 1)\zeta} \right)^{1/3} \tag{47}$$

transforms Eq. 46 to

$$\frac{d^2 \theta_i}{d\lambda^2} + 3\lambda^2 \frac{d\theta_i}{d\lambda} = 0 \tag{48}$$

The boundary conditions, Eqs. 44, become

$$\theta_i(\lambda = 0) = 1 \tag{49a}$$

$$\theta_i(\lambda = \infty) = 0 \tag{49b}$$

The solution to Eq. 48 with these boundary conditions is

$$\theta_i = \frac{1}{\Gamma(4/3)} \int_\lambda^\infty \exp(-\lambda^3)\, d\lambda \tag{50}$$

The flux to the electrode is found by

$$N_i = -D_i \left. \frac{\partial c_i}{\partial x} \right|_{x=0} = -D_i (c_i^\infty - c_i^0) \left. \frac{d\theta_i}{d\lambda} \right|_{\lambda=0} \frac{\partial \lambda}{\partial \xi} \frac{d\xi}{dx} \tag{51}$$

$$= \frac{-D_i (c_i^\infty - c_i^0)}{\Gamma(4/3)} \left(\frac{2av_c}{9D_i \eta_c} \right)^{1/3} \left(\frac{1}{y^2 + a^2} \right)^{1/3} \left(\frac{1}{z} \right)^{1/3} \tag{52}$$

Equivalent Velocity of Rising Cylinder. The only quantity in Eq. 52 still to be specified is v_c, the cylinder velocity. There are

three possibilities:

1. Equate the volumetric flow rate of the cylinder to that of the rising bubbles,
2. Equate the drag on the rising cylinder to the drag on the rising bubbles,
3. Allow the cylinder to rise at the terminal velocity of the individual bubbles

The first option allows for no entrainment of the liquid by the rising bubbles, the second for intermediate entrainment, and the third for maximum entrainment. This last possibility can be eliminated by noting that v_c would not depend on bubble evolution rate, but only on bubble size, which is not the case (see Figure 15).

Equating the gas flows for the cylinder and the bubble stream, option 1, we find

$$v_c = \frac{\dot{V}}{\pi R_b^2} = \frac{IRT}{n_g F p \pi R_b^2} \tag{53}$$

and the mass-transfer rate due to the rising cylinder is dependent on $I^{1/3}$.

In option 2, the case of equal drag forces, the drag on the cylinder can be calculated by integrating the tangential force over the area of the cylinder. It is simpler, however, to calculate the drag on the wall (which must be equivalent since the wall is infinite). The drag on the wall per cylinder length l is:

$$\frac{F_D}{l} = 2\int_0^\infty \mu \left.\frac{\partial v_z}{\partial x}\right|_{x=0} dy \tag{54}$$

Substituting Eq. 45 for $\partial v_z/\partial x|_{x=0}$ into Eq. 54 we obtain

$$\frac{F_D}{l} = \frac{4 a v_c \mu}{\eta_c}\int_0^\infty \frac{1}{y^2 + a^2}\, dy \tag{55}$$

$$= \frac{a v_c \mu}{\eta_c}\frac{1}{a}\tan^{-1}\frac{y}{a}\Big|_{y=0}^{y=\infty} \tag{56}$$

$$\frac{F_D}{l} = \frac{2\mu v_c \pi}{\eta_c} \tag{57}$$

The drag on a series of bubbles is computed by assuming that the bubbles act independently and rise in Stokes flow. Faxén (1923) solved for the total drag force on a single bubble rising at terminal velocity v_t and distance L from a wall:

$$\frac{F_D}{\text{bubble}} = \frac{6\pi\mu R_b v_t}{f(R_b/L)} \tag{58}$$

where $f(R_b/L)$ is the correction for the presence of the wall and is given by (Happel and Brenner, 1965, p. 327)

$$f\left(\frac{R_b}{L}\right) = 1 - \frac{9}{16}\left(\frac{R_b}{L}\right) + \frac{1}{8}\left(\frac{R_b}{L}\right)^3 - \frac{45}{256}\left(\frac{R_b}{L}\right)^4 - \frac{1}{16}\left(\frac{R_b}{L}\right)^5 \tag{59}$$

The frictional drag force per unit length of a rising column of bubbles is the product of the frictional drag force per bubble (⅔ of the total drag force) and the bubble frequency, divided by the bubble velocity:

$$\frac{F_D}{l} = \frac{F_D}{\text{bubble}}\frac{\dot{V}}{\frac{4}{3}\pi R_b^3 v_t} = \frac{3\mu\dot{V}}{R_b^2 f(R_b/L)} \tag{60}$$

Combining Eqs. 60 and 57, we finally obtain

$$v_c = \frac{\dot{V}}{\pi R_b^2}\frac{3\eta_c}{2 f(R_b/L)} = \frac{IRT}{n_g F p \pi R_b^2}\frac{3\eta_c}{2 f(R_b/L)} \tag{61}$$

In the above treatment we have chosen, somewhat arbitrarily, to exclude the form drag from the bubble force calculation. By this choice we attempt to account for the fact that the bubbles do not act independently: each bubble decreases the form drag on the bubble that follows.

We have also chosen to fix the radius of the cylinder (at the radius of the bubbles), and to vary the cylinder velocity. If we had done the reverse, we would have obtained the same result in the maximum entrainment case, option 3. In the case of equivalent volumetric flow rate, option 1, we would have obtained only a weak dependence on bubble evolution rate. In the case of equivalent drag, option 2, we would have obtained the identical result as that derived above, Eq. 61.

The average mass-transfer enhancement due to the rising cylinder is evaluated in terms of the average current density by

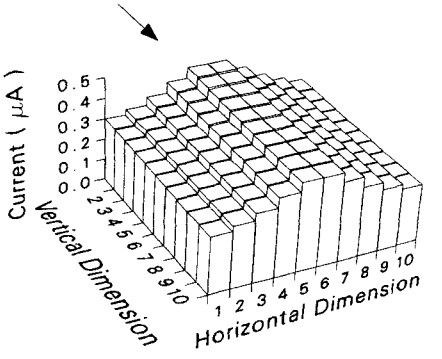

Figure 19a. 200 μm rise.

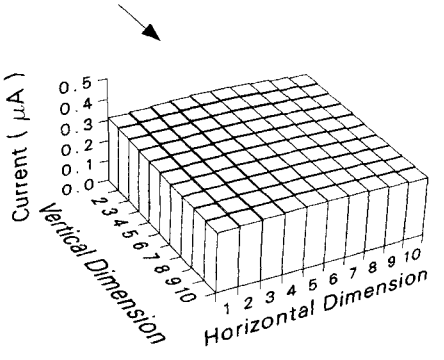

Figure 19b. 750 μm rise.

Figure 19. Mass transfer distributions resulting from 100 μm dia. cylinder rising from electrode surface at equivalent of 30 μA rate of gas evolution. Background natural convection current is included.

integrating Eq. 52 over the electrode area:

$$i_{avg} = \frac{-n_i F D_i (c_i^{\infty} - c_i^0)}{s_i \Gamma(4/3)} \left(\frac{2av_c}{9D_i\eta_c}\right)^{1/3} \times \frac{3}{2}\left[\frac{z_2^{(2/3)} - z_1^{(2/3)}}{z_2 - z_1}\right]\frac{1}{y_2 - y_1}\int_{y_1}^{y_2}\left(\frac{1}{y^2 + a^2}\right)^{1/3} dy \quad (62)$$

with v_c given by Eq. 53 or Eq. 61.

The predicted current distribution resulting from a rising cylinder that is equivalent, on the basis of equivalent drag, to a 30 μA bubble stream at 200 μm is shown in Figure 19. Also shown is the current distribution resulting from a stream of the same diameter and rise velocity, but positioned at 750 μm. The distributions in Figure 19 include the background natural-convection mass-transfer, added according to Eq. 30, so that they may be compared directly with the experimentally measured current distributions shown in Figure 12. The degree of uniformity in the calculated and experimental distributions agrees reasonably well, although the comparison is obscured by the additional nonuniformity induced in the experimental data by nonfunctioning segments. The agreement between the calculated and experimental average mass-transfer enhancement is excellent. Figure 20 compares, as a function of bubble evolution rate, the experimental and calculated mass transfer rates for a bubble-stream-to-wall separation of 200 μm. The calculated results for both equivalent drag, Eq. 61, and equivalent volumetric flow of gas, Eq. 53, are shown. The former matches experiment very well; the latter would be expected to present a lower limit to the mass-transfer enhancement. The functionality of the dependence of mass transfer enhancement on bubble evolution rate is seen to agree with the 1/3 power dependence predicted by the model. This result implies that the enhancement is due to a laminar flow of gas and liquid. Figure 21 shows the same comparison for a separation of 300 μm and Figure 22 for a separation of 450 μm. Least-squares fits of the three log i vs. log I curves give exponential dependences of 0.31, 0.28, and 0.34 for 200, 300, and 450 μm, respectively. The agreement in magnitude of mass-transfer rate between experiment and theory decreases with increasing separation. In part this reflects a weakness of the theory, but also, as the total mass-transfer rate

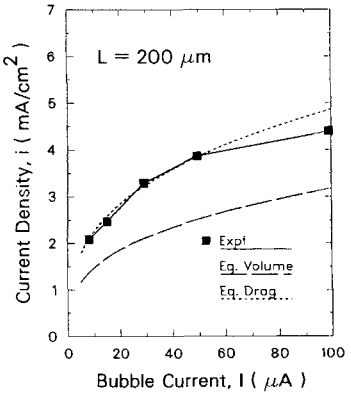

Figure 20. Mass transfer enhancement as a function of bubble evolution rate.

Enhancement (1) measured for a single stream of bubbles; (2) calculated for a steadily rising cylinder, both centered 200 μm from electrode

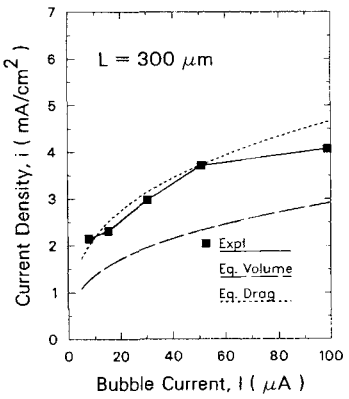

Figure 21. Mass transfer enhancement as in Figure 20, 300 μm from electrode.

approaches the background natural-convection mass-transfer rate, the sensitivity of the determined value of the enhancement to experimental error increases.

In summary, the rising cylinder model describes the effect of an increased laminar flow along the electrode and neglects individual bubble effects. The resulting mass-transfer rate matches the experimentally measured values in both magnitude and distribution. The measured dependence of the mass-transfer enhancement on the bubble-stream-to-electrode separation is stronger than predicted by the cylinder model.

Conclusions

The mass-transfer enhancement due to a stream of bubbles rising along a vertical electrode has been characterized by transient and spatial resolution using an indicator ion reaction at a micromosaic electrode. Bubbles rising within the mass-transfer boundary layer create a strong, localized, periodic enhancement. Spatial resolution of these effects supports a surface-renewal mechanism of mass-transfer enhancement. The effective renewal path of the bubbles is typically five to seven bubble diameters wide.

Bubble streams rising outside the mass-transfer boundary layer cause a steady increase in the mass-transfer rate over a large area. The mass-transfer enhancement in this case depends on the bubble evolution rate to the 1/3 power, the result of an increased velocity gradient at the electrode surface. The experi-

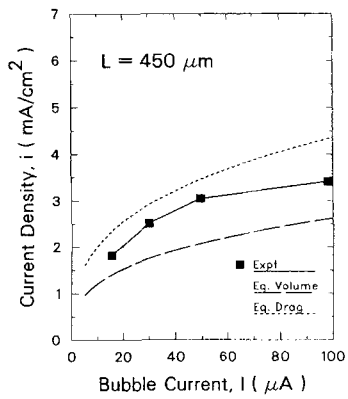

Figure 22. Mass transfer enhancement as in Figure 20, 450 μm from electrode.

mental results are consistent with a laminar-flow model that treats the rising column of bubbles and entrained liquid as an equivalent cylinder rising with the same friction drag.

Acknowledgment

The authors are grateful for the generous contribution of both time and effort on the part of Hewlett-Packard Company and AT&T Bell Laboratories in the design and fabrication of the micromosaic electrodes. This work was supported by the Assistant Secretary of Conservation and Renewable Energy, Office of Energy Systems Research, Energy Storage Division of the U.S. Department of Energy under Contract No. DE-AC03-76SF00098. Gina Whitney received fellowship support from the National Science Foundation and the Exxon Education Foundation.

Notation

a = constant of geometry, Eq. 33, cm
b = slope of i vs. $1/w$, Eq. 29
c_i = concentration of indicator ion, mol/cm^3
d = bubble dia. or equivalent channel dia., cm
D_i = diffusivity of indicator ion, cm^2/s
f = dimensionless y coordinate
F = Faraday constant, 96,487 C/eq
F_D = drag force, g · cm/s^2
Gr = Grashof number
H = electrode length, cm
i = current density, A/cm^2
i_{avg} = current density, averaged over electrode area, A/cm^2
I = bubble evolution rate, A
i_{nc} = natural-convection current density, A/cm^2
i_{max} = current density to renewal path, A/cm^2
k = mass-transfer coefficient, cm/s
l = cylinder length, cm
L = distance between wall and bubble column or cylinder, cm
n_i = number of electrons transferred in indicator reaction
n_g = number of electrons transferred in gas evolution reaction
$\dot{n}_z$ = cumulative bubble evolution rate below height z, s^{-1}
n/A = number of bubbles evolved per unit area, cm^{-2}
N = flux, mol/cm^2 · s
$\overline{N}$ = flux averaged over time, mol/cm^2 · s
$\overline{N}_A$ = flux averaged over time and area, mol/cm^2 · s
$\overline{N}_\tau$ = flux averaged over waiting time, mol/cm^2 · s
$\overline{N}_{\tau,A}$ = flux averaged over waiting time and area, mol/cm^2 · s
p = pressure, atm
Pe = Peclet number, $v_c a/D_i$
R = universal gas constant, 82.055 cm^3 · atm/mol · K
R_b = bubble radius, cm
R_c = cylinder radius, cm
Re = Reynolds number, $v_c a/\nu$
s = fraction of surface renewed per time, s^{-1}
s_i = stoichiometric coefficient of indicator ion in electrode reaction
Sc = Schmidt number, ν/D_i
Sh = Sherwood number, dimensionless mass flux
t = time, s
T = temperature, K
u = liquid velocity, cm/s
v = gas evolution rate per unit area, cm^3/cm^2 · s
$\mathbf{v}$ = liquid velocity, cm/s
v_z = fluid velocity, cm/s
v_z^* = fluid velocity, made dimensionless with v_c
v_t = terminal velocity of rising bubble, cm/s
$\dot{V}$ = volumetric gas evolution rate, cm^3/s
w = electrode width, cm
x = horizontal distance from electrode surface, cm
y = horizontal distance along electrode surface, cm
z = vertical distance along electrode surface, cm

Greek letters

δ = diffusion boundary-layer thickness, cm
ϵ = gas volume fraction
ζ = dimensionless z coordinate
η_c = constant of geometry, Eq. 34
θ = fraction of electrode area shadowed by attached bubbles
θ_i = dimensionless concentration of indicator ion
λ = similarity variable, Eq. 47
μ = viscosity, g/cm · s
ν = kinematic viscosity, cm^2/s
ξ = dimensionless x coordinate
ρ = density, g/cm^3
τ_w = waiting time between bubble departure and nucleation, s

Subscripts and superscripts

i = indicator ion
0 = at electrode surface
∞ = in bulk solution

Literature Cited

Alkire, R., and P-Y. Lu, "Effect of Hydrogen Evolution on Current Distribution During Electrodeposition at Vertical Electrodes," *J. Electrochem. Soc.*, **126,** 2118 (1979).

Beck, T. R., "A Contribution to the Theory of Electrolytic Chlorate Formation," *J. Electrochem. Soc.*, **116,** 1038 (1969).

Churchill, S. W., "A Comprehensive Correlating Equation for Laminar, Assisting, Forced and Free Convection," *Am. Inst. Chem. Eng. J.*, **23,** 10 (1977).

Cottrell, F. G., "Der Reststrom bei galvanischer Polarisation, betrachtet als ein Diffusionsproblem," *Zeitschrift für Physikalische Chemie,* **42,** 385 (1903).

Danckwerts, P. V., "Significance of Liquid-Film Coefficients in Gas Absorption," *Ind. Eng. Chem.*, **43,** 1460 (1951).

Dees, D, W., *"Mass Transfer at Gas-Evolving Surfaces in Eletrolysis,"* Ph.D. Thesis, Univ. California, Berkely, (also Lawrence Berkeley Lab. Rept. LBL-16176) (1983).

Dees, D. W., and C. W. Tobias, "Experimental Studies of Free-Convection Mass Transfer to a Horizontal Surface with a Micro-Mosaic Electrode," *J. Electrochem. Soc.*, **134,** 369 (1987a).

———, "Mass Transfer at Gas-Evolving Surfaces: A Microscopic Study," *J. Electrochem. Soc.*, **134,** 1702 (1987b).

———, "A Novel Micro-Mosaic Electrode for the Study of Transport Phenomena at Gas-Evolving Electrodes," *Extend. Abs. 33d Int. Soc. Electrochem. Meet.*, **1,** 456 (1982).

Economou, D. J., and R. C. Alkire, "Two-Phase Mass Transfer in Channel Electrolyzers with Gas-Liquid Flow," *J. Electrochem. Soc.*, **132,** 601 (1985).

Faxén, H., "Die Bewegung einer starren Kugel längs der Achse eines mit zäher Flüssigkeit gefüllten Rohres," *Arkiv för Matematik, Astronomi och Fysik,* **17**(27), 1 (1923).

Fouad, M. D., and G. H. Sedahmed, "Effect of Gas Evolution on the Rate of Mass Transfer at Vertical Electrodes," *Electrochim. Acta,* **17,** 665 (1972).

———, "Mass Transfer at Horizontal Gas-Evolving Electrodes," *Electrochim. Acta,* **18,** 55 (1973).

Green, M., and P. H. Robinson, "Kinetics of the Cathodic Reduction of Anions," *J. Electrochem. Soc.*, **106,** 253 (1959).

Happel, J., and H. Brenner, *Low Reynolds Number Hydrodynamics,* Prentice-Hall, Englewood Cliffs, NJ (1965).

Higbie, R., "The Rate of Absorption of a Pure Gas into a Still Liquid During Short Times of Exposure," *Trans. Am. Inst. Chem. Eng.*, **31,** 365 (1935).

Ibl, N., and J. Venczel, "Untersuchung des Stofftransports an gasentwickelnden Elektroden," *Metalloberfläche,* **24,** 366 (1970).

Ibl, N., E. Adam, J. Venczel, and E. Schalch, "Stofftransport bei der Elektrolyse mit Gasrührung," *Chem. Ing. Technik,* **43,** 202 (1971).

Janssen, L. J. J., "Mass Transfer at Gas-Evolving Electrodes," *Electrochim. Acta,* **23,** 81 (1978).

Janssen, L. J. J., and E. Barendrecht, "The Effect of Electrolytic Gas Evolution on Mass Transfer at Electrodes," *Electrochim Acta,* **24,** 693 (1979).

Janssen, L. J. J., and J. G. Hoogland, "The Effect of Electrolytically Evolved Gas Bubbles on the Thickness of the Diffusion Layer," *Electrochim. Acta,* **15,** 1013 (1970).

———, "The Effect of Electrolytically Evolved Gas Bubbles on the

Thickness of the Diffusion Layer. II," *Electrochim. Acta,* **18,** 543 (1973).
Kind, R., "Untersuchung des Stofftransports und der Rührwirkung bei gasentwickelnden Elektroden," Diss., ETH, Zurich (1975).
Landau, U., and C. W. Tobias, "Mass Transport and Current Distribution in Channel-Type Electrolyzers in the Laminar and Turbulent Flow Regimens," *Extend. Abst. No. 266, 159th Meet. Electrochem. Soc.,* Washington DC (May, 1976).
Roald, B., and W. Beck, "The Dissolution of Magnesium in Hydrochloric Acid," *J. Electrochem. Soc.,* **98,** 277 (1951).
Ruckenstein, E., and R. Rajagopalan, "A Simple Algebraic Method for Obtaining the Heat or Mass Transfer Coefficients Under Mixed Convection," *Chem. Eng. Commun.,* **4,** 15 (1980).
Rousar, I., J. Kaćin, E. Lippert, F. Smirous, and V. Cezner, "Transport of Heat or Mass to a Electrode in the Region of Hydrogen Evolution. II," *Electrochim. Acta,* **20,** 295 (1975).
Sides, P. J., "Phenomena and Effects of Electrolytic Gas Evolution," *Modern Aspects of Electrochemistry, No. 18,* R. E. White, J. O'M. Bockris, B. E. Conway, eds., Plenum, New York, 303 (1986).
Stephan, K., and H. Vogt, "A Model for Correlating Mass Transfer Data at Gas-Evolving Electrodes," *Electrochim. Acta,* **24,** 11 (1979).
Venczel, J., "Über den Stofftransport an gasentwickelnden Elektroden," Diss., ETH, Zurich (1961).
Vogt, H., "Ein Beitrag zum Stoffübergang an gasentwickelnden Elektroden," Diss., Univ. of Stuttgart (1977).
———, "Gas-Evolving Electrodes," *Comprehensive Treatise of Electrochemistry,* E. Yeager, J. O'M. Bockris, B. E. Conway, S. Sarangapani, eds., Plenum, New York, **6,** 445 (1983).
Vondrak, J., and J. Balej, "Influence of Mercury on Hydrogen Overvoltage on Solid Metal Electrodes. I," *Electrochim. Acta,* **15,** 1653 (1970).
Whitney, G. M., "*Microscale Resolution of Interfacial Mass-Transfer Rates in Electrode Processes,*" Ph.D. Thesis, Univ. California, Berkeley, (also Lawrence Berkeley Lab. Rept. LBL-23596) (1987).
Whitney, G. M., and C. W. Tobias. "The Onset of Buoyancy-Induced Convection at a Micro-Mosaic Electrode," *J. Electroanalyt. Chem. Interf. Electrochem.,* **229,** 429 (1987).
Zuber, N., "Nucleate Boiling. The Region of Isolated Bubbles and the Similarity with Natural Convection," *Int. J. Heat Mass Transf.,* **6,** 53 (1963).

Manuscript received Oct. 26, 1987, and revision received July 18, 1988.